JACS
JOURNAL OF THE AMERICAN CHEMICAL SOCIETY
pubs.acs.org/JACS
Article

A Single-Phase Mixed Ion-Electron Conducting Metal–Organic Framework

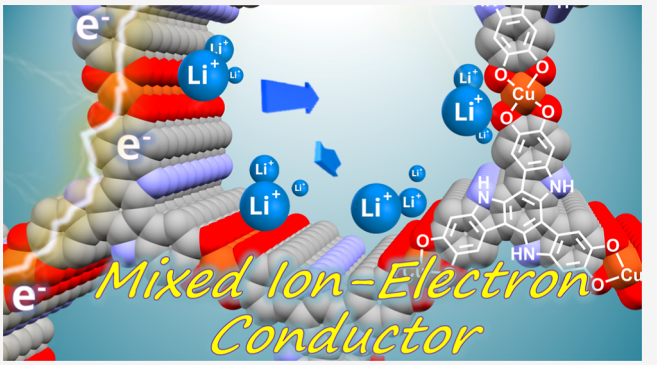
Petru Apostol,* Xiaodong Lin, Simon M.-M. Dubois, Yan Zhang, Robert Markowski, Xiaolong Guo, Jiande Wang, Wenjie Shi, Laura Caputo, Da Tie, Viliam Frano, Darsi Rambabu, Vasudeva Rao Bakuru, Koen Robeyns, Mircea Dincă, Pulickel M. Ajayan, Jean-Christophe Charlier, and Alexandru Vlad*

Cite This: J. Am. Chem. Soc. 2026, 148, 4339–4348

Read Online

ACCESS | Metrics & More | Article Recommendations | Supporting Information

ABSTRACT: Mixed ionic-electronic conductors (MIECs) are highly sought after for electrochemical systems because they support concurrent charge and mass transport. Yet, structurally well-defined single-phase MIECs remain scarce, as most systems rely on physical mixtures of ionic and electronic conductors. Here, we introduce a cation-rich design strategy to realize solid-state mixed Li^+-electronic conduction in a two-dimensional copper–catecholate metal–organic framework, $Cu_3(HOTAT)_2$, built from the 3-fold symmetric new ligand 2,3,7,8,12,13-hexahydroxytriazatruxene (HHTAT). Owing to the combined redox activity of Cu^{2+}/Cu^+ and the HOTAT ligand, controlled fractional reduction generates a family of $Li_xCu_3(HOTAT)_2$ ($0 \le x \le 7.50$) phases with tunable transport properties, in good agreement with electronic-structure calculations. The Li-rich phase $Li_{7.50}Cu_3(HOTAT)_2$ exhibits intrinsic mixed conduction at room temperature, with an electronic conductivity of 2.8×10^{-3} S cm^{-1}, and solid-state Li^+ conductivity of 1.1×10^{-3} S cm^{-1}. As a proof of concept, $Li_{7.50}Cu_3(HOTAT)_2$ operates as a homogeneous cathode in all-solid-state Li batteries, delivering 100 mAh g^{-1} after 100 cycles with ~99.8% Coulombic efficiency, indicative of highly reversible electrochemical behavior. These results establish cation-rich reduction of redox-active 2D MOFs as an efficient route to engineer solid-state mixed Li^+-electronic conductors, opening a pathway toward dual-conducting porous materials for solid-state electrochemical technologies.



INTRODUCTION

Mixed ionic-electronic conductors (MIECs) enable the concurrent transport of ionic and electronic charge carriers. This mixed conductivity is well established in ceramic systems such as $SrTiO_3$, TiO_2, CeO_2, perovskite-type oxides,[1] garnet-type oxides,[2] and sulfides.[3] Moreover, battery electrode materials are, by definition, also MIECs,[4] since electrochemical energy storage requires simultaneous ion and electron transport. Although such dual transport is essential for fast and efficient operation, limited ionic or electronic conduction remains a technological limitation. Owing to their ability to transport both carrier types, MIECs are essential for technologies spanning energy storage,[5] fuel and electrochemical cells, electrocatalysis, sensors, and smart materials.[6] Despite this broad relevance, identifying single-phase MIECs with a controlled and well-defined structure remains challenging; in many practical cases, the targeted balance between ionic and electronic transport is achieved through heterogeneous composites or multiphase architectures.[7,8]

Organic mixed ionic-electronic conductors (OMIECs) have therefore emerged as an important complementary materials class, offering structural compliance, redox tunability, abundant feedstocks, and low-temperature processing.[9] In OMIECs, mixed conduction typically arises from either (i) ions that are tethered (directly or indirectly) to a conjugated backbone or (ii) mobile ions introduced during processing or operation, whose motion is coupled to electronic carriers through doping and charge compensation. In such systems, ionic and electronic contributions can vary strongly with composition, morphology, applied potential, and percolation effects often govern the effective transport. While these features have enabled major advances, many OMIECs intrinsically rely on ion solvation and swelling in liquid/gel environments, motivating the search for solid-state,[10,11] structurally defined platforms where mixed conduction can be engineered at the molecular level.

Metal–organic frameworks (MOFs) provide such a platform, as they have been shown to exhibit either ionic

Received: October 14, 2025
Revised: January 14, 2026
Accepted: January 16, 2026
Published: January 22, 2026



Downloaded via UNIV CATHOLIQUE DE LOUVAIN on February 20, 2026 at 15:06:47 (UTC).
See https://pubs.acs.org/sharingguidelines for options on how to legitimately share published articles.

© 2026 American Chemical Society

https://doi.org/10.1021/jacs.5c18105
J. Am. Chem. Soc. 2026, 148, 4339–4348

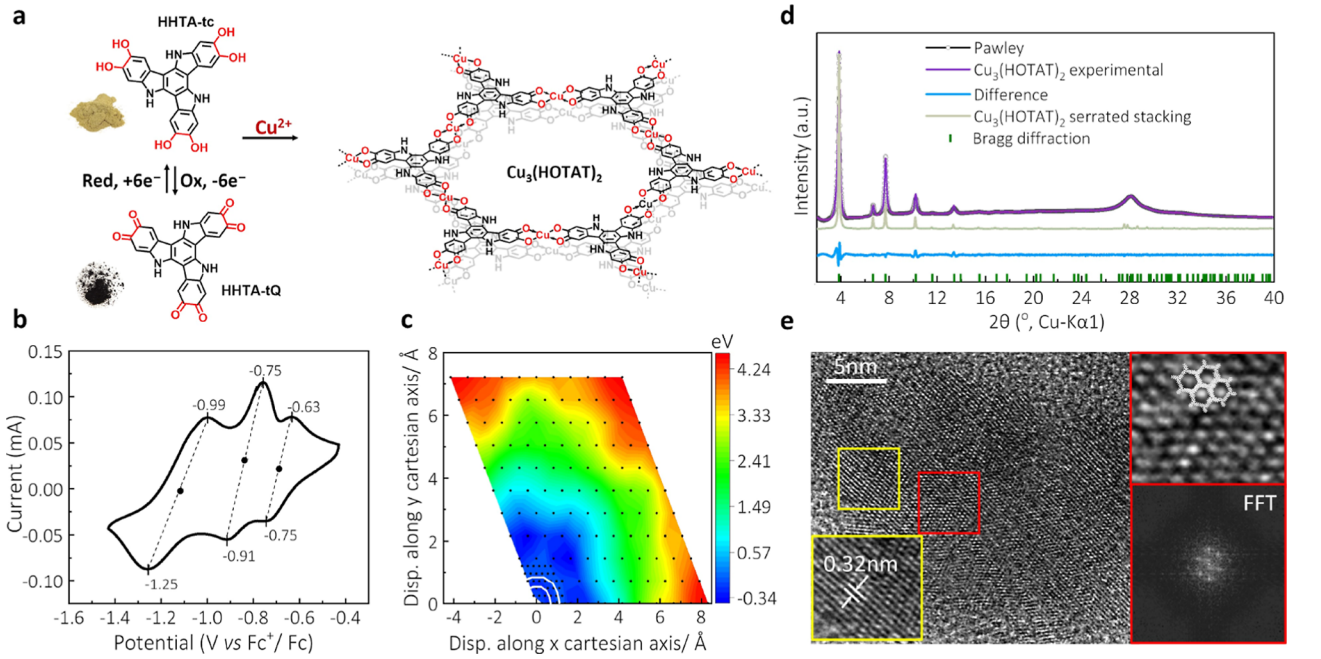


Figure 1. (a) Synthetic scheme and structure of $Cu_3(HOTAT)_2$. Optical micrograph insets display the morphology and color of the HHTAT ligand in different oxidation states. (b) Cyclic voltammetry of Li_6HOTAT. Measurement conditions are 2 mM active material dissolved in DMSO with 0.1 M LiCl, 100 mV s^{-1}, Pt disk working electrode, potential calibrated versus Fc^+/Fc internal reference. (c) Density functional theory (DFT) calculated 2D color contour plots of the potential energy surface of $Cu_3(HOTAT)_2$ as a function of interlayer translation. Black dots indicate the specific configurations, where total energies were explicitly computed. Energies are referenced to the eclipsed configuration. White contour lines highlight the region where the system is stabilized by more than 125 meV relative to the eclipsed stacking. (d) Experimental, Pawley refined, and simulated PXRD patterns for $Cu_3(HOTAT)_2$. (e) High-magnification HRTEM images of $Cu_3(HOTAT)_2$ with fast Fourier transform analysis of the corresponding areas indicated by red squares (imaged along the *c* direction).

conductivity[12,13] or electronic conductivity,[14] enabled by modular metal−linker design and permanent porosity. In particular, two-dimensional MOFs are notable electronic conductors and offer rich redox tunability, where conductivity can be modulated through redoxhopping and band-like transport; such redox-state changes can arise during synthesis or be induced by postsynthetic modification.[15−19] However, most conductive MOFs reported to date are predominantly either electronic or ionic conductors, and integrating both functionalities within a single crystalline, structurally defined phase remains synthetically nontrivial. Achieving intrinsic mixed ion-electron transport in one MOF requires the simultaneous realization of an electronically delocalized conduction network and a population of mobile ions that are only weakly bound and experience a comparatively flat potential-energy landscape.

Here, we propose a cation-rich strategy to realize mixed Li^+−electronic transport in a 2D MOF. Starting from an intrinsically electronically conducting framework, we generate a delocalized, anionic lattice through controlled reduction, wherein the charge compensation is realized by the incorporation of Li^+ that do not serve a rigid structural role. We hypothesize that this combination, electronic delocalization in the 2D framework together with loosely bound countercations within the porous lattice, can create a single-phase (solid-state) mixed conductor. According to the above-mentioned rationale, we analyzed the redox properties of $Cu_3(HOTAT)_2$ MOF, constructed from the new π-extended ligand 2,3,7,8,12,13-hexahydroxytriazatruxene (HHTAT). This material exhibits an intrinsic electronic conductivity of 0.160 S cm^{-1}, and structural stability during reversible redox exchange involving nearly 9 electrons (e^-) per formula unit. Controlled fractional reduction of $Cu_3(HOTAT)_2$ yielded a series of compositions with variable Li content ($Li_xCu_3(HOTAT)_2$, wherein x = 0.85, 2.45, 5.50, and 7.50). In these phases, the Cu(II) node is gradually reduced to Cu(I), whereas the *o*-semiquinone (sQ^-) units of HOTAT are reduced to *o*-catecholate (Q^{2-}), resulting in a $Li_3[Cu^IO_4]^{3-}$ node. The gradual framework reduction and Li-cation incorporation are found to lower the electronic conductivity, in accordance with the measured optical band gap and theoretical computation revealing electronic structural changes. The Li-rich $Li_{7.50}Cu_3(HOTAT)_2$ phase is found to exhibit MIEC property, with electronic and ionic conductivities of $\sigma_e = 2.8 \times 10^{-3}$ S cm^{-1} and $\sigma_{Li^+} = 1.1 \times 10^{-3}$ S cm^{-1}, as confirmed by various measurement techniques. As proof of concept, this MIEC phase was evaluated as a single component active material battery electrode and enabled all-solid-state lithium batteries to achieve stable cycling for over 100 cycles, with the highest attained discharge specific capacities at 60 °C of 140 mAh g^{-1} corresponding to 61% of material utilization. These findings represent the first example of a coupled electronic-ionic conducting single-phase 2D-MOF, providing a foundation for the design of new dual-conducting MOFs and their application in solid-state electronic and energy devices.

RESULTS AND DISCUSSION

Synthesis and Characterization of $Li_xCu_3(HOTAT)_2$, x = 0, 0.85, 2.45, 5.50, and 7.50

Oxidation of 5,6-dihydroxyindole in acidic aqueous media led to a hexahydroxytriazatruxene isomer mixture, 2,3,7,8, 12,13-hexamethoxytriazatruxene, and 2,3,6,7,11,12-hexamethoxytria-

https://doi.org/10.1021/jacs.5c18105
J. Am. Chem. Soc. 2026, 148, 4339−4348

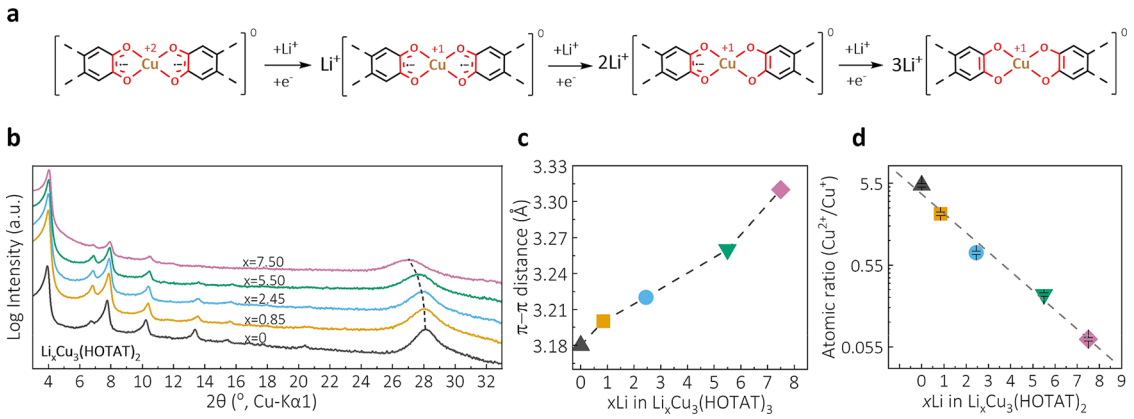


Figure 2. (a) Schematic of the stepwise lithiation process in the secondary building unit $[Cu^{II}O_4]^0 \rightarrow Li_3[Cu^{I}O_4]^{3-}$. (b) PXRD of lithiated $Li_xCu_3(HOTAT)_2$, x = 0, 0.85, 2.45, 5.50, and 7.50 phases. (c) Evolution of atomic Cu^{2+}/Cu^+ ratio and (d) evolution of the interlayer spacing for studied $Li_xCu_3(HOTAT)_2$ phases.

zatruxene. Isolating the C_3-symmetric, 2,3,7,8, 12,13-hexahydroxytriazatruxene (HHTAT) proved to be difficult due to its inherently poor solubility.[20] Accordingly, we synthesized HHTAT through a new method involving the trimerization of 5,6-dimethoxyindolin-2-one in $POCl_3$. The isomeric products were separated by selective precipitation of the N-Boc-protected C_3-symmetric intermediate, 2,3,7,8,12,13-hexamethoxytriazatruxene $(MeO)_6$-TAT$(Boc)_3$, from the reaction mixture. Subsequently, deprotection of this intermediate led to the desired HHTAT product in high yield (refer to the Supporting Information for details, Figures S1−S7). Single-crystal X-ray analysis revealed that HHTAT crystallizes in its reduced form with C_3-symmetry (Figure S8 and Table S1). The redox activity of the Li_6HOTAT version (refer to the Supporting Information for experimental and synthesis details, Figure S9) was studied by cyclic voltammetry in 0.1 M LiCl in DMSO. Three reversible, two-electron processes at −1.12, −0.83, and −0.69 V (versus Fc^+/Fc) are observed (Figure 1a,b), and are attributed to the semiquinoid redox couples.

Reaction of $Cu(OAc)_2{\cdot}H_2O$ and HHTAT in a 3:1 DMI/H_2O solvent mixture under air at 65 °C yielded $Cu_3(HOTAT)_2$ black powder consisting of irregularly shaped particles measuring between 50 and 200 nm, as determined by scanning electron microscopy (Figure S10). The Powder X-ray diffraction pattern (PXRD) of $Cu_3(HOTAT)_2$ (Figure 1d) revealed a set of prominent peaks at 2θ (Cu Ka_1) = 3.83°, 6.63°, 7.69°, 10.19°, 13.37°, and 28.11°, which, according to Pawley refinement, were fitted in the hexagonal space group *P6* with unit cell parameters of $a = b = 26.6365$ and $c = 3.17$ Å. The strong diffraction [001] peak at 28.11° is representative of high long-range order along the c direction with a calculated interlayer spacing d_{001} of 3.17 Å. Density functional theory (DFT) calculations (Table S2) reveal that $Cu_3(HOTAT)_2$ is unstable in its eclipsed stacking configuration. The most favorable conformations correspond instead to serrated stacking. An isotropic in-plane translation of ∼0.5 Å was found to stabilize the system by more than 125 meV relative to the eclipsed phase (Figure 1c), with the associated PXRD patterns displaying good agreement with experiment (Figures 1d, S11). Interestingly, some larger interlayer translations yield deeper energy minima, but the corresponding PXRD patterns were found to deviate substantially from the experimental data, indicating that these theoretical energy valleys are not realized in the actual material. High-resolution transmission electron microscopy of $Cu_3(HOTAT)_2$ revealed that the sample is composed of crystalline domains, confirming the honeycomb framework. Further inspection indicates an additional periodic $\pi-\pi$ feature with a spacing of 0.32 nm (Figure 1e, inset), in good agreement with the Pawley refinement for the c unit cell parameter. The N_2 adsorption isotherm revealed a Brunauer−Emmett−Teller (BET) surface area of 862 $m^2\ g^{-1}$ with a corresponding BJH adsorption cumulative pore volume of 0.25 $cm^3\ g^{-1}$ (Figure S12). The large BET surface area isamong the highest values reported for copper-based 2D-e-MOFs and 2D-MOF analogues.[16]

Gradual chemical reduction of $Cu_3(HOTAT)_2$ was performed through the controlled addition of varying equivalents of lithium naphthalenide ($Li^+[C_{10}H_8^{\bullet -}]$, $E_{1/2}$ = −3.10 V versus Fc^+/Fc)[21] to a suspension of MOF in dry tetrahydrofuran (THF) to achieve $Li_xCu_3(HOTAT)_2$ x = 0, 0.85, 2.45, 5.50, and 7.50 phases (Figure 2a). Powder X-ray diffraction (PXRD) data revealed that the reaction is topotactic for all levels of reduction with no noticeable changes in the low angle PXRD peaks, except the diminished intensity of the main peaks (Figure 2b). The interlayer distance increases with the extent of lithiation from 3.17 Å for pristine $Cu_3(HOTAT)_2$ to 3.20 Å, 3.22 Å, 3.26 Å, and 3.31 Å for $Li_{0.85}Cu_3(HOTAT)_2$, $Li_{2.45}Cu_3(HOTAT)_2$, $Li_{5.50}Cu_3(HOTAT)_2$, and $Li_{7.50}Cu_3(HOTAT)_2$, respectively, as calculated from the [001] peak reflection between 2θ = 26° and 28° (Figure 2c). Given the effective ionic radius of Li^+ (0.9 Å, without solvation shell),[22] the moderate d_{001} expansion is unlikely to arise solely from intercalation between MOF layers. It is plausible that Li^+ is predominantly accommodated in the MOF pores near catecholate redox sites, although partial interlayer occupation cannot be excluded at a high Li content. Increased negative charge density upon reduction may drive interlayer expansion via electrostatic repulsion between adjacent anionic layers and/or between Li^+ populations associated with neighboring sheets. Partial occupation of the pores is further confirmed by a progressive decrease in surface area, with $Li_{2.45}Cu_3(HOTAT)_2$ and $Li_{7.50}Cu_3(HOTAT)_2$ nevertheless maintaining permanent porosity, with BET surface areas of 732 and 266 $m^2\ g^{-1}$, respectively (Figure S12).

X-ray photoelectron spectroscopy (XPS) analysis of the Cu 2p region in the pristine MOF revealed the presence of two distinct copper species: Cu $2p_{3/2}$ peaks at 931 and 932 eV, corresponding to Cu^+ and Cu^{2+} oxidation states. The relative

https://doi.org/10.1021/jacs.5c18105
J. Am. Chem. Soc. 2026, 148, 4339−4348

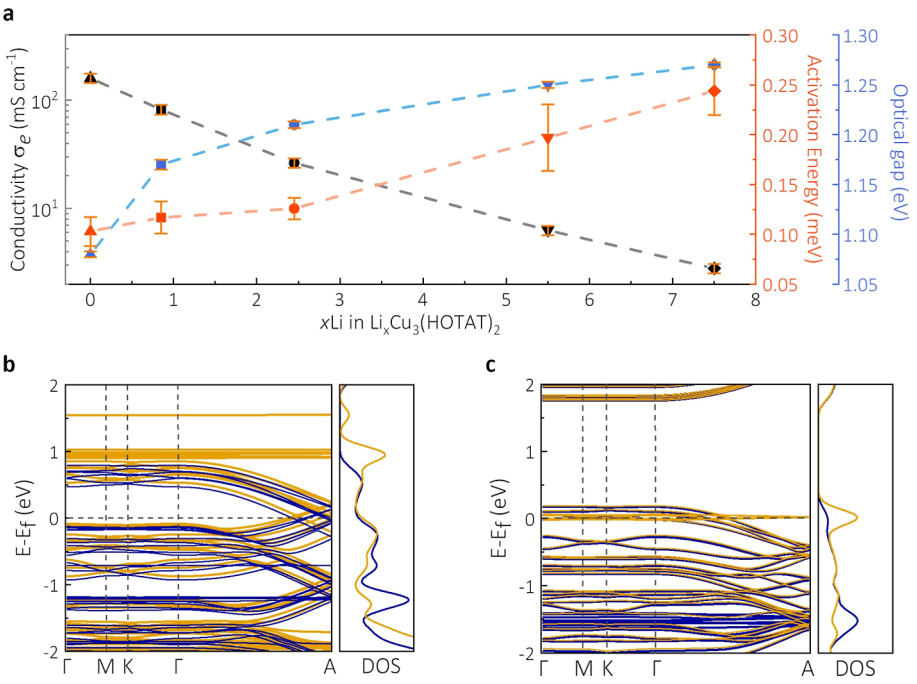


Figure 3. Charge transport properties of $Cu_3(HOTAT)_2$ and $Li_xCu_3(HOTAT)_2$ x = 0, 0.85, 2.45, 5.50, and 7.50 MOF phases. (a) Conductivity data, activation energy (E_a), and optical band gap at different degrees of lithiation. Error bars represent the standard deviation of three measurements. Computed spin-resolved band structures of bulk $Cu_3(HOTAT)_2$ (b) and $Li_6Cu_3(HOTAT)_2$ (c), with majority- and minority-spin states shown in blue and orange, respectively. The corresponding density of states (DOS) is displayed alongside each band structure. Energies are referenced to the Fermi level (set to 0 eV). Lithiation leads to the opening of an energy gap, as highlighted by the DOS.

composition was determined to be 83.9 at % Cu^{2+} and 16.1 at % Cu^+ ± 2%, indicating an initial Cu^{2+}-rich phase (equivalent of ≈2.5 Cu^{2+} and ≈0.5 Cu^+ ions per $Cu_3(HOTAT)_2$ unit). Upon reduction, deconvolution of the Cu $2p_{3/2}$ region[23] showed a progressive reduction of Cu^{2+}, particularly in the Li-rich phase, with only 6.3 at % Cu^+ ± 2% retained (equivalent of ≈0.2 Cu^{2+}; and ≈2.8 Cu^+ ions in $Li_{7.50}Cu_3(HOTAT)_2$; refer to Figures 2d, S13, and Table S3). Fourier-transform infrared spectroscopy analysis (FTIR) revealed vanishing characteristic stretching vibrations of carbonyl ($\nu_{C=O}$ at 1612 cm^{-1}) and the emergence of a broad vibration band of the ν_{C-OLi} at 1040 cm^{-1} with progressively increasing intensity upon reaching the $Li_{7.50}Cu_3(HOTAT)_2$ composition. As the lithium content increases, the intensity and width of the Cu−O vibration band (i.e., 450−550 cm^{-1})[24] decrease significantly, due to increased disorder of square planar geometry and weakening of Cu−O stretching vibrations associated with the decreasing Cu^{2+}:Cu^+ ratio (Figure S14).

The electron paramagnetic resonance (EPR) spectra of the pristine $Cu_3(HOTAT)_2$ demonstrate a broad and asymmetric line shape (Figure S15), arising from strong spin−spin exchange interactions of the unpaired electron primarily residing in a metal-centered orbital of Cu^{2+} (S = 1/2). The g-value was determined to be ∼2.09, consistent with previous reports on copper-based MOF.[25,26] Upon reduction to $Li_{0.85}Cu_3(HOTAT)_2$, the EPR signal increases in intensity, and a narrow EPR line (ΔHpp = 0.904 mT) appears, centered at 3508.8 G (g = 2.0010). This behavior indicates a significant increase in radical concentration within a more covalent electronic environment, while the Cu^{2+} ionis are reduced to diamagnetic Cu^+, which is EPR silent. The g-value of this radical signal agrees well with that observed for the benzo-semiquinone form.[27] Upon further reduction, the EPR signal maintains a similar shape, but its intensity decreases slightly, suggesting a transformation from the $[Cu^I(C_4O_4)]^{2-}$ radical to $[Cu^I(C_4O_4^-)]^{3-}$. Considering that most of the Cu^{2+} ions are reduced to Cu^+, the unsaturated quinoidal rings play a dominant role in accepting electrons and forming a closed-shell, π-conjugated aromatic network $[Cu^I(C_4O_4^-)]^{3-}$, as illustrated in Figure 2a. These results are consistent with the FTIR and XPS analysis and similar evolution of the EPR signal has been observed in other carbonyl-based redox materials.[28,29]

The synthesis and chemical reduction of pristine $Cu_3(HOTAT)_2$ implies the use of various solvents systems (H_2O, DMI, and THF), with the retention of solvent possible within the framework given the high surface areas attained. Complete desolvation occurred only at elevated temperatures, accompanied by partial degradation, as evidenced from thermogravimetric analysis (TGA, Figure S16). Microelemental analysis of desolvated phases revealed residual solvents trapped within the frameworks, with higher content of solvent for Li-rich compositions (Figure S14 and Table S4). FTIR analysis revealed an increase in the intensity of the THF stretching bands (ν_{THF} = 2958 cm^{-1} and 2868 cm^{-1}) with increased lithium content, which may suggest the presence of partially solvated Li^+ ions within the activated MOF structure. However, even for the Li-rich phase, a total of 4 THF molecules per $Li_{7.50}Cu_3(HOTAT)_2$ formula unit were identified (Table S4). Considering that a solvated Li-cation holds on average 3 to 4 molecules of solvent in the solvation sheath, full and even partial solvation of Li^+ in these phases can be excluded, while also considering that some THF molecules could be physiosorbed within the porous matrix.

Charge Transport Analysis in $Li_xCu_3(HOTAT)_2$

The room-temperature electrical conductivities of $Cu_3(HOTAT)_2$ and lithiated phases were measured by two-contact probe measurements on cold-pressed polycrystalline

https://doi.org/10.1021/jacs.5c18105
J. Am. Chem. Soc. 2026, 148, 4339−4348

samples. Pristine $Cu_3(HOTAT)_2$ exhibits a conductivity of 0.160 S cm^{-1}, whereas upon lithiation, the electrical conductivity gradually decreased to 82×10^{-3} S cm^{-1} for $Li_{0.85}Cu_3(HOTAT)_2$, 26×10^{-3} S cm^{-1} for $Li_{2.45}Cu_3(HOTAT)_2$, and 2.8×10^{-3} S cm^{-1} for $Li_{7.50}Cu_3(HOTAT)_2$ (Figure 3a). All phases display thermally activated transport with gradual increase in activation energy (E_a) upon lithiation (Figures 3a, S17). The relatively high E_a observed for the $Li_{7.50}Cu_3(HOTAT)_2$ phase (0.244 eV), compared to the pristine $Cu_3(HOTAT)_2$ (0.103 eV), indicates that charge transport is dominated by thermally activated hopping rather than delocalized band conduction. This is attributed to the reduced state of the ligand upon lithiation, which localizes electronic states and inhibits band-like transport.

To understand the origin of the modulation in conductivity, diffuse-reflectance ultraviolet−visible−near IR (DRUV−vis−NIR) spectroscopy was used. The diffuse reflectance spectrum of $Cu_3(HOTAT)_2$ exhibits absorption bands at 3.34 and 2.00 eV that are maintained upon reduction to $Li_xCu_3(HOTAT)_2$ (Figure S18). The bands at 3.34 eV, assigned to ligand-centered charge transfer, diminish in intensity upon framework reduction as a consequence of increased valence delocalization. The most prominent transition for reduced phases is a ligand-to-metal charge transfer band, which undergoes a blue shift from 1.74 to 2.00 eV, indicating changes in the electronic structure upon reduction.[30−32] Extracting optical gaps (E_0) from the DRUV−vis spectra by plotting the data in the Tauc coordinate reveals that E_0 increases gradually with lithium content in MOFs from 1.08 eV forpristine $Cu_3(HOTAT)_2$ to 1.27 eV for $Li_{7.50}Cu_3(HOTAT)_2$. This trend correlates well with the observed decrease in electrical conductivity, supporting the presence of continuous compositional band changes (Figure 3a).

We also performed ultraviolet photoelectron spectroscopy (UPS) on the pristine and lithiated MOF samples to probe the Fermi-level alignment (position of the Fermi level relative to the valence band maximum, E_F-E_V) and doping type, Figure S19. The pristine $Cu_3(HOTAT)_2$ exhibits an E_F-E_V value of 0.32 ± 0.03 eV, indicative of a semiconducting character with the Fermi level located slightly above the valence band edge. Low degrees of lithiation ($Li_{0.85}Cu_3(HOTAT)_2$ and $Li_{2.45}Cu_3(HOTAT)_2$) induce minor changes, with E_F-E_V values of 0.44 ± 0.03 eV and 0.46 ± 0.03 eV, respectively, suggesting that the introduction of a small amount of lithium has a limited impact on the intrinsic electronic structure. In stark contrast, lithium-rich phases display a pronounced upward shift of the Fermi level, with E_F-E_V increasing to 0.72 ± 0.03 eV in $Li_{5.50}Cu_3(HOTAT)_2$ and to 0.83 ± 0.03 eV in $Li_{7.50}Cu_3(HOTAT)_2$. This indicates electron donation from lithium at high loading levels, revealing *n*-type doping and a transition toward a strongly electron-rich electronic configuration. The magnitude of the E_F-E_V shift in these phases suggests the emergence of new electronic states or reorganization of the band structure. Altogether, the UPS data reveal a two-regime lithiation process: a low-Li region in which the band structure remains largely unperturbed, and a high-Li region characterized by pronounced electronic restructuring and substantial Fermi level elevation.

Density functional theory (DFT) calculations were next used to provide insight into the electronic structure of $Cu_3(HOTAT)_2$ and the origin of the changes in conductivity upon lithiation. In the pristine phase, band-structure analysis reveals highly dispersive itinerant bands crossing the Fermi level, enabling extended conduction both in-plane and out-of-plane, consistent with the experimentally measured conductivities. Along the stacking direction (A−Γ), metallic behavior is predicted, while in-plane (Γ−K−M), the Fermi level lies within a gap, suggesting semiconducting behavior that matches the experimentally determined in-plane optical band gap (Figure 3b). Upon lithiation, the electronic bands progressively narrow and lose dispersion (Figure 3c). This reduction is most pronounced along the stacking direction, consistent with weaker interlayer orbital overlap (Figure 2d) and the observed loss of interlayer conduction pathways. In the Li-rich phase, orbital projections of the DFT eigenstates (Figures S20 and S22) reveal two distinct classes of bands near the Fermi energy: (i) a very narrow, spin-minority band with almost exclusive Cu-3d character and (ii) broader bands predominantly associated with the carbon framework of the HOTAT ligands. Inverse participation ratio analysis confirms that the Cu-derived band is strongly localized on individual Cu centers, while the framework bands remain delocalized across the MOF layers (Figure S22). Additionally, the computed eigenstate velocities (Figure S23) show that the Cu-3d band pinned at the Fermi level carries negligible velocity and, therefore, contributes essentially no coherent spectral weight. Only the ligand-derived bands provide itinerant channels contributing to coherent transport. This indicates that the localized Cu-3d states may act as trap states, suppressing transport through scattering and carrier localization. In this scenario, transport becomes dominated by thermally activated hopping rather than coherent band conduction, consistent with the strong suppression of experimental conductivity.

The reduction of coherent spectral weight and the concurrent emergence of Cu-centered localization predicted by DFT rationalize the observed experimental trends: (i) the monotonic decay of conductivity with increasing Li content, (ii) the increase in thermal activation energy, and (iii) the widening optical gap (Figure 3a). While the predicted optical-gap evolution deviates from the linearity expected in Tauc plots (Figure S18), such discrepancies may arise from experimental sample-related effects, mixed-valent Cu states (Figure 2c), or structural disorder.[33−35] Electronic population analyses further support this scenario. Mulliken analysis shows a slight increase in Cu-3d occupancy (≈9.38 → 9.53 e^-/Cu) and a reduction of local spin (≈0.70 → 0.45 μB) upon insertion of 2Li per Cu, consistent with a partial reduction of Cu centers. Hirshfeld and Voronoi charges both report modest electron gain on Cu nodes (≈0.06−0.07 e^- per Cu), corroborating the Mulliken results but indicating that the majority of Li-donated electrons are localized on the ligand π/O states rather than fully reducing $Cu^{2+} \rightarrow Cu^+$, pointing toward a mixed metal−ligand reduction mechanism. Overall, combined experimental and theoretical analyses reveal that the decline in conductivity upon lithiation of $Cu_3(HOTAT)_2$ arises from several interconnected factors. XPS data show a gradual reduction of Cu^{2+} to Cu^+ as lithium is introduced, altering the electronic structure of the material (Figures 2c, S13, and Table S3). In the pristine phase, Cu^{2+} centers facilitate delocalized charge transport; however, their reduction to Cu^+ increases the level of electron localization, thereby reducing carrier mobility. It is reasonable to assume that concurrent ligand reduction contributes to a more localized charge distribution, leading to an increased band gap. This interpretation aligns well with both the UV−vis DR analysis

https://doi.org/10.1021/jacs.5c18105
J. Am. Chem. Soc. 2026, 148, 4339−4348

and theoretical predictions. Altogether, the expansion of interlayer distance, Cu^{2+} reduction, and emergence of localized states collectively lead to diminished bulk conductivity, especially in the Li-rich phase. These findings highlight the intricate interplay among structural evolution, redox behavior, and charge transport in $Cu_3(HOTAT)_2$.

Mixed Ion-Electron Transport in $Li_{7.50}Cu_3(HOTAT)_2$ and Use as Neat Electrode Material

Whereas intermediate Li-containing phases were found to display low ionic conductivity, with the exact quantification impeded by the high electronic conductivity retained (Figures S24 and S25, refer to the Experimental Section and Supporting Information for the ionic and electronic measurements details), the Li-rich $Li_{7.50}Cu_3(HOTAT)_2$ phase was found to exhibit comparable range mixed conductivities. The PEIS of $Li_{7.50}Cu_3(HOTAT)_2$ displays a depressed semicircle (Figures 4a, S26),[36] with the low-frequency component corresponding

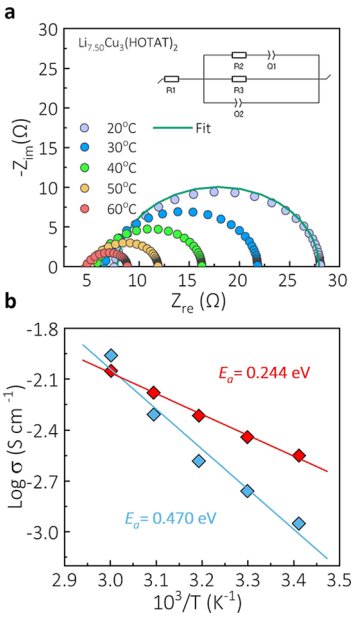


Figure 4. Mixed ion-electron conductivity analysis of $Li_{7.50}Cu_3(HOTAT)_2$. (a) Nyquist plots of the a.c. PEIS data profiles at selected temperatures and (b) Arrhenius plot of electrical (σ_e, red) and ionic conductivity (σ_{Li}^+, blue) for the $Li_{7.5}Cu_3(HOTAT)_2$ phase.

to the electronic resistance (R_e), with values consistent with those obtained from d.c. I–V measurements (Table S5). The high-frequency response in turn reflects the combined contributions of ionic and electronic conductivity (see Experimental Procedures for details). At 293 K, the electronic and ionic conductivities (σ_e and σ_{Li}^+) of $Li_{7.50}Cu_3(HOTAT)_2$ were estimated to be 2.8×10^{-3} S cm^{-1} and 1.1×10^{-3} S cm^{-1}, respectively. Both σ_e and σ_{Li}^+ exhibit Arrhenius-type temperature dependence, with activation energies (E_a) of 0.244 eV for electronic transport and 0.470 eV for ionic transport (Figure 4b). $Li_{7.50}Cu_3(HOTAT)_2$ exhibits an ionic conductivity that is approximately 1 order of magnitude higher than that of a recently single-phase MIEC benchmarks reported for inorganic sulfides while maintaining a lower but still significant electronic conductivity[3] and surpassing the MIEC properties for garnet-type oxide materials.[2] These differences highlight the distinct conduction balance of this MOF-based single-phase architecture. However, many systems rely on multiphase or composite architectures (i.e., either inorganic or organic), which complicates direct benchmarking. It is worth being pointed out that at 60 °C, high mixed conductivity values of $\sigma_e = 1 \times 10^{-2}$ S cm^{-1} and $\sigma_{Li}^+ = 1 \times 10^{-2}$ S cm^{-1} are attained, with the ionic conductivity, for instance, comparable to Li–ion liquid electrolytes (measured at room temperature)[37] and surpassing any previous report on liquid/solvent free MOF ionic conductor.[13] To verify the ionic transport properties, a complementary electron-blocking DC polarization method was used to measure the ionic conductivity directly. A five-layer symmetric cell with the configuration SS | Li | Li_6PS_5Cl | $Li_{7.50}Cu_3(HOTAT)_2$| Li_6PS_5Cl | Li | SS was assembled, where Li_6PS_5Cl (LPSCl) serving as the electron-blocking layer (Figure S27). The resulting ionic conductivity of $Li_{7.50}Cu_3(HOTAT)_2$ was determined to be 1.3×10^{-3} S cm^{-1}, in good agreement with the value obtained from PEIS measurements (1.1×10^{-3} S cm^{-1}).

Given the robust nature of $Cu_3(HOTAT)_2$ upon redox, with stability retained after nearly 7.5-electron reduction, as well as its intrinsic electronic conduction properties, the charge storage performances of $Cu_3(HOTAT)_2$ were assessed next. First, neat $Cu_3(HOTAT)_2$ electrodes were tested in conventional liquid electrolyte cells (1 M LiTFSI in DOL/DME). The galvanostatic charge/discharge curves of the $Cu_3(HOTAT)_2$ measured within a potential window of 1.7–3.5 V vs Li^+/Li, exhibit initial discharge and charge capacities of 184 mAh g^{-1} and 217 mAh g^{-1} (Figure 5a). After five activation cycles, the material achieved a specific capacity of 225 mAh g^{-1}, close to the theoretical 9-electron transfer capacity of 228 mAh g^{-1}, at a cycling rate of 0.01 A g^{-1} (C/20) (Figure 5b). Lithiated phases were also tested, and during the initial charging step, specific capacities consistent with their lithium content were found. These results confirm the reversible extraction of Li^+ ions from the MOF (Figure 5c). The neat $Cu_3(HOTAT)_2$ electrode also shows excellent rate capability, and even at a high rate of 2.3 A g^{-1} (10C), the electrode can deliver a capacity of 169 mAh g^{-1} (75% of the initial capacity, with minimal polarization, Figure 5b,d). Long-term cycling at 0.2 A g^{-1} (1C) show good capacity retention of 73% over 270 cycles, 167 mAh g^{-1}, with high Coulombic efficiency (99.8% in average, Figure 5d).

An interesting observation is the wider electrochemical stability window of $Cu_3(HOTAT)_2$ compared to the analogous $Cu_3(HHTP)_2$. While the latter shows stable storage of only 3-electrons,[38,39] $Cu_3(HOTAT)_2$ is found to reversibly store up to 9-electrons, while being also stable in a wider electrochemical window of 0.01–3.5 V vs Li^+/Li (Figure S28). This is attributed to the unique characteristics of this MOF, $Cu_3(HOTAT)_2$, where the ligand participates in the redox process along with Cu^{2+}/Cu^+ redox couple (mixed cation-ligand redox, supported by ex situ FTIR, and ex situ XPS analysis, Figures 2a, S29–S31). In both, pristine and after one full discharge–charge states, a distinct carbonyl stretching vibration ($\nu_{C=O}$) is observed in the 1672–1570 cm^{-1} region, confirming the oxidized form of the catechol moiety.[38,40] Upon reduction, this band vanishes, indicating the conversion of C=O to C–O bonds, supporting the redox active nature of the linker. Additionally, the appearance of a pronounced ν_{C-OLi} peak (1047 cm^{-1}) in the reduced (lithiated) state provides further evidence for lithium–ion coordination to the oxygen atoms of the catechol groups (Figure S30). Ex situ XPS analyses further prove mixed redox of the Cu^{2+}/Cu^+ couple as well as C=O/C–O bond interconversion (Figure S31).

https://doi.org/10.1021/jacs.5c18105
J. Am. Chem. Soc. 2026, 148, 4339–4348

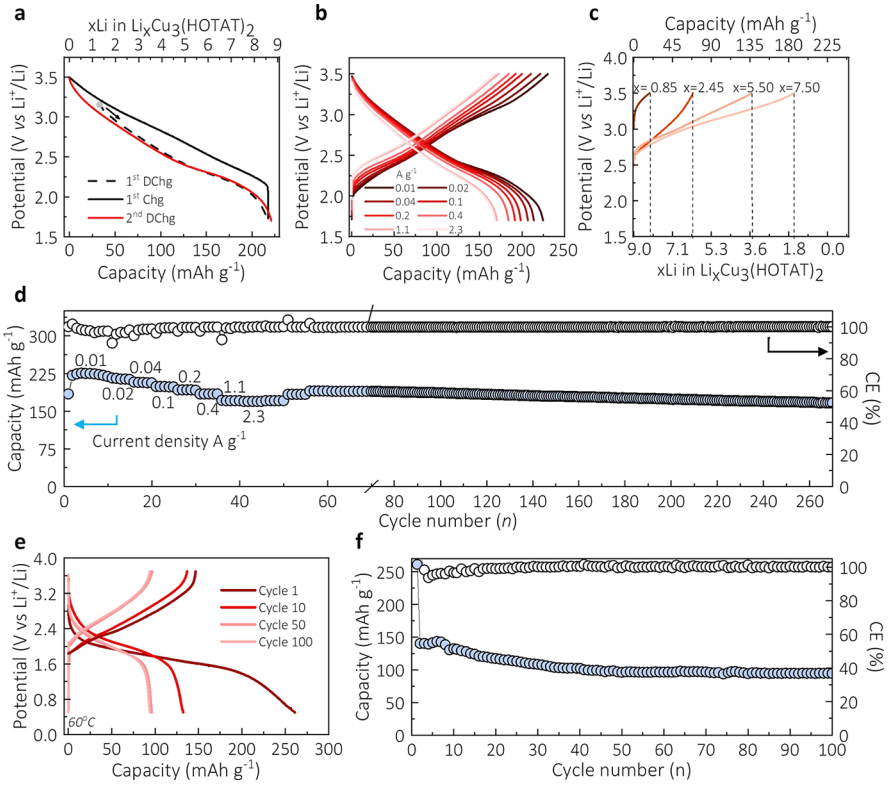


Figure 5. Charge-storage performances of $Cu_3(HOTAT)_2$ and $Li_{7.50}Cu_3(HOTAT)_2$. (a,b) Galvanostatic charge−discharge profiles for the $Cu_3(HOTAT)_2$ neat electrode in 1 M LiTFSI in DOL/DME electrolyte at the initial cycles and different current densities. (c) First galvanostatic charge profile for $Li_xCu_3(HOTAT)_2$ phases. (d) Long-term cycling stability along with the capacity−rate test for the neat $Cu_3(HOTAT)_2$ electrode. (e,f) Cycling performance of a solid-state cell with neat $Li_{7.50}Cu_3(HOTAT)_2$ at a current density of 30 mA g^{-1} at 60 °C and corresponding long-term cycling stability.

Finally, considering the MIEC properties of $Li_{7.50}Cu_3(HOTAT)_2$, we also tested this phase as a sole component in a solid-state lithium cell. To assess first the chemical reactivity and stability between the $Li_{7.50}Cu_3(HOTAT)_2$ and LPSCl, a composite mixture in a ratio of 1:1 (by mass) was analyzed by FTIR. No noticeable changes were observed, confirming the chemical compatibility of $Li_{7.50}Cu_3(HOTAT)_2$ with LPSCl (Figure S32).[41] The cell construct consisted of LPSCl as a solid electrolyte, lithium metal as negative, and $Li_{7.50}Cu_3(HOTAT)_2$ as a neat positive electrode material (no electrolyte, conductive or binder additives were added). At 60 °C, the cell was cycled between 3.7 and 0.6 V vs Li^+/Li with a current density of 30 mA g^{-1}. After initial cycles activation, a capacity retention of 140 mAh g^{-1} was attained (corresponding to 61% of material utilization, theoretical capacity of 228 mAh g^{-1}) with a slight decline to 100 mAh g^{-1} after 100 cycles (71% of the initial capacity), while maintaining a stable charge−discharge potential profile (Figure 5e,f). To evaluate the stability of the cathode, ex situ FTIR and PXRD analyses were performed on the recovered sample after 100 cycles. The ex situ FTIR spectra of $Li_{7.50}Cu_3(HOTAT)_2$ before and after cycling exhibit no significant changes in the characteristic vibrational bands, apart from minor variations in band intensities. The postcycling PXRD pattern shows that the overall layered MOF is largely preserved, with only peak broadening indicating slight structural disorder but no substantial framework degradation. These results confirm that the chemical structure of the framework remains intact during repeated lithiation−delithiation cycles (Figure S33). The lower materials utilization as compared to the liquid cell construct can be explained by the higher complexity of the system and the generation of various interphases, as well as Li-cation-dependent electronic and ionic conductivity of $Li_xCu_3(HOTAT)_2$ phases. Nevertheless, the stable voltage, high average Coulombic efficiency (99.8%), and limited capacity decay suggest the reversible nature of $Li_xCu_3(HOTAT)_2$ phase upon Li-cation uptake and release in solid-phase.

CONCLUSIONS

We demonstrate a cation-rich design strategy to realize solid-state, single-phase mixed ion-electron conduction in a structurally defined 2D MOF. Starting from the intrinsically electronically conducting Cu−catecholate framework $Cu_3(HOTAT)_2$, controlled reduction enables progressive Li^+ incorporation to form $Li_xCu_3(HOTAT)_2$ (x = 0.85, 2.45, 5.50, and 7.50), accompanied by coupled reduction of the Cu nodes ($Cu^{2+} \rightarrow Cu^+$) and catechol redox units. This compositional series reveals how the Cu^{2+}/Cu^+ ratio and ligand redox state tune the electronic percolation while simultaneously enabling Li^+ transport in the same phase. The Li-rich $Li_{7.5}Cu_3(HOTAT)_2$ composition exhibits clear solid-state MIEC behavior at room temperature (σ_e = 2.8 × 10^{-3} S cm^{-1}, σ_{Li^+} = 1.1 × 10^{-3} S cm^{-1}), metrics confirmed by complementary transport analysis techniques. As a proof of concept, $Li_{7.5}Cu_3(HOTAT)_2$ functions as a homogeneous, additive-free electrode material in an all-solid-state Li cell, delivering stable cycling beyond 100 cycles. Overall, these results define key chemical requirements for MOF-based

https://doi.org/10.1021/jacs.5c18105
J. Am. Chem. Soc. 2026, 148, 4339−4348

MIECs: an electronically connected framework, a multielectron redox reservoir for cation compensation, and weak/frustrated cation binding; and provide a modular blueprint for engineering tunable mixed conduction in porous crystalline solids.

■ ASSOCIATED CONTENT

Supporting Information

The Supporting Information is available free of charge at https://pubs.acs.org/doi/10.1021/jacs.5c18105.

Additional experimental details, materials, and methods, including photographs of experimental setup, data analysis, and discussion (PDF)

Accession Codes

Deposition No. 2484266 contains the supplementary crystallographic data for this paper. These data can be obtained free of charge via the joint Cambridge Crystallographic Data Centre (CCDC) and Fachinformationszentrum Karlsruhe Access Structures service.

■ AUTHOR INFORMATION

Corresponding Authors

Petru Apostol − *Institute of Condensed Matter and Nanosciences, Université Catholique de Louvain, Louvain-la-Neuve B-1348, Belgium;* orcid.org/0009-0005-3123-6029; Email: petru.apostol@uclouvain.be

Alexandru Vlad − *Institute of Condensed Matter and Nanosciences, Université Catholique de Louvain, Louvain-la-Neuve B-1348, Belgium; WEL Research Institute, Wavre 1300, Belgium;* orcid.org/0000-0002-0059-9119; Email: alexandru.vlad@uclouvain.be

Authors

Xiaodong Lin − *Institute of Condensed Matter and Nanosciences, Université Catholique de Louvain, Louvain-la-Neuve B-1348, Belgium;* orcid.org/0000-0002-1867-4789

Simon M.-M. Dubois − *Institute of Condensed Matter and Nanosciences, Université Catholique de Louvain, Louvain-la-Neuve B-1348, Belgium*

Yan Zhang − *Institute of Condensed Matter and Nanosciences, Université Catholique de Louvain, Louvain-la-Neuve B-1348, Belgium*

Robert Markowski − *Institute of Condensed Matter and Nanosciences, Université Catholique de Louvain, Louvain-la-Neuve B-1348, Belgium*

Xiaolong Guo − *Institute of Condensed Matter and Nanosciences, Université Catholique de Louvain, Louvain-la-Neuve B-1348, Belgium*

Jiande Wang − *Department of Chemistry, Massachusetts Institute of Technology, Cambridge 02139-4307 Massachusetts, United States*

Wenjie Shi − *Institute for New Energy Materials & Low Carbon Technologies, Tianjin University of Technology, Tianjin 300384, China*

Laura Caputo − *Institute of Condensed Matter and Nanosciences, Université Catholique de Louvain, Louvain-la-Neuve B-1348, Belgium;* orcid.org/0000-0003-0185-9442

Da Tie − *Institute of Condensed Matter and Nanosciences, Université Catholique de Louvain, Louvain-la-Neuve B-1348, Belgium*

Viliam Frano − *Institute of Condensed Matter and Nanosciences, Université Catholique de Louvain, Louvain-la-Neuve B-1348, Belgium*

Darsi Rambabu − *Institute of Condensed Matter and Nanosciences, Université Catholique de Louvain, Louvain-la-Neuve B-1348, Belgium*

Vasudeva Rao Bakuru − *Institute of Condensed Matter and Nanosciences, Université Catholique de Louvain, Louvain-la-Neuve B-1348, Belgium*

Koen Robeyns − *Institute of Condensed Matter and Nanosciences, Université Catholique de Louvain, Louvain-la-Neuve B-1348, Belgium;* orcid.org/0000-0002-4763-4217

Mircea Dincă − *Department of Chemistry, Massachusetts Institute of Technology, Cambridge 02139-4307 Massachusetts, United States;* orcid.org/0000-0002-1262-1264

Pulickel M. Ajayan − *Department of Materials Science and Nanoengineering, Rice University, Houston 77005 Texas, United States;* orcid.org/0000-0001-8323-7860

Jean-Christophe Charlier − *Institute of Condensed Matter and Nanosciences, Université Catholique de Louvain, Louvain-la-Neuve B-1348, Belgium*

Complete contact information is available at: https://pubs.acs.org/10.1021/jacs.5c18105

Notes

The authors declare no competing financial interest.

■ ACKNOWLEDGMENTS

Support was received from the European Research Council under the European Union's Horizon 2020 research and innovation program (grant agreement No. 770870, MOOiRE). D.R., X.L., and B.V.R. acknowledge F.R.S.-FNRS for Chargé de Recherché (CR) fellowship (grant agreement Nos. 40010410, 40023657). R.M. acknowledges F.R.S.-FNRS for Ph.D. fellowship. D.T., X.G., and Y.Z. acknowledge CSC for the Ph.D. fellowships. X.L. acknowledges financial support from the Marie Skłodowska-Curie Actions (grant agreement no. 101064286) for his postdoctoral fellowship. Research in the Dinca lab was supported by the U.S. Department of Energy, Office of Science, Basic Energy Sciences, under award #DE-SC0023288. This work was also supported by the National Natural Science Foundation of China (22201209 and 22571227); the Natural Science Foundation of Tianjin City (25JCQNJC00480); Fédération Wallonie-Bruxelles through ARC Dreams Grants (N° 21/26-116); EOS project CONNECT (N° 40007563); and the Belgium F.R.S. FNRS through the research project (T.029.22F). Computational resources were provided by the supercomputing facilities of the Université catholique de Louvain (CISM) and the Consortium des Équipements de Calcul Intensif en Fédération Wallonie Bruxelles (CÉCI) funded by the Fonds de la Recherche Scientifique de Belgique (F.R.S.-FNRS) under the convention N° 2.5020.11.

REFERENCES

(1) Teraoka, Y.; Zhang, H. M.; Okamoto, K.; Yamazoe, N. Mixed Ionic-Electronic Conductivity of La1−xSrxCo1−yFeyO3−δ Perovskite-Type Oxides. *Mater. Res. Bull.* **1988**, *23* (1), 51−58.

(2) Jin, Z.; Kong, X.; Huang, H.; Jiang, Y.; Xiang, W.; Xu, Y.; Zhang, L.; Peng, R.; Wang, C. Garnet-Type Solid-State Mixed Ionic and Electronic Conductor. *Energy Storage Mater.* **2023**, *59*, 102788.

(3) Cui, L.; Zhang, S.; Ju, J.; Liu, T.; Zheng, Y.; Xu, J.; Wang, Y.; Li, J.; Zhao, J.; Ma, J.; Wang, J.; Xu, G.; Chan, T.-S.; Huang, Y.-C.; Haw, S.-C.; Chen, J.-M.; Hu, Z.; Cui, G. A Cathode Homogenization Strategy for Enabling Long-Cycle-Life All-Solid-State Lithium Batteries. *Nat. Energy* **2024**, *9* (9), 1084−1094.

(4) Park, M.; Zhang, X.; Chung, M.; Less, G. B.; Sastry, A. M. A Review of Conduction Phenomena in Li-Ion Batteries. *J. Power Sources* **2010**, *195* (24), 7904−7929.

(5) Snook, G. A.; Kao, P.; Best, A. S. Conducting-Polymer-Based Supercapacitor Devices and Electrodes. *J. Power Sources* **2011**, *196* (1), 1−12.

(6) Chen, C.-C.; Fu, L.; Maier, J. Synergistic, Ultrafast Mass Storage and Removal in Artificial Mixed Conductors. *Nature* **2016**, *536* (7615), 159−164.

(7) Choi, G. M.; Kim, J. H.; Park, Y. M. Electrical Conductivity of Ionic and Electronic Mixture. *MRS Online Proc. Libr.* **2001**, *699* (1), 96.

(8) Lin, Y.; Fang, S.; Su, D.; Brinkman, K. S.; Chen, F. Enhancing Grain Boundary Ionic Conductivity in Mixed Ionic−Electronic Conductors. *Nat. Commun.* **2015**, *6* (1), 6824.

(9) Paulsen, B. D.; Tybrandt, K.; Stavrinidou, E.; Rivnay, J. Organic Mixed Ionic−Electronic Conductors. *Nat. Mater.* **2020**, *19* (1), 13−26.

(10) Fabiano, S.; Flagg, L.; Hidalgo Castillo, T. C.; Inal, S.; Kaake, L. G.; Kayser, L. V.; Keene, S. T.; Ludwigs, S.; Muller, C.; Savoie, B. M.; Lüssem, B.; Lutkenhaus, J. L.; Matta, M.; Meli, D.; Patel, S. N.; Paulsen, B. D.; Rivnay, J.; Surgailis, J. On the Fundamentals of Organic Mixed Ionic/Electronic Conductors. *J. Mater. Chem. C* **2023**, *11* (42), 14527−14539.

(11) Park, M.; Ju, H.; Oh, J.; Park, K.; Lim, H.; Yoon, S. M.; Song, I. Proton-Electron Coupling and Mixed Conductivity in a Hydrogen-Bonded Coordination Polymer. *Nat. Commun.* **2025**, *16* (1), 1316.

(12) Lim, D.-W.; Kitagawa, H. Proton Transport in Metal−Organic Frameworks. *Chem. Rev.* **2020**, *120* (16), 8416−8467.

(13) Zhang, Y.; Wang, J.; Apostol, P.; Rambabu, D.; Eddine Lakraychi, A.; Guo, X.; Zhang, X.; Lin, X.; Pal, S.; Rao Bakuru, V.; Chen, X.; Vlad, A. Bimetallic Anionic Organic Frameworks with Solid-State Cation Conduction for Charge Storage Applications. *Angew. Chem., Int. Ed.* **2023**, *62* (42), No. e202310033.

(14) Xie, L. S.; Skorupskii, G.; Dincă, M. Electrically Conductive Metal−Organic Frameworks. *Chem. Rev.* **2020**, *120* (16), 8536−8580.

(15) Wang, L.; Sarkar, A.; Grocke, G. L.; Laorenza, D. W.; Cheng, B.; Ritchhart, A.; Filatov, A. S.; Patel, S. N.; Gagliardi, L.; Anderson, J. S. Broad Electronic Modulation of Two-Dimensional Metal−Organic Frameworks over Four Distinct Redox States. *J. Am. Chem. Soc.* **2023**, *145* (15), 8486−8497.

(16) Apostol, P.; Gali, S. M.; Su, A.; Tie, D.; Zhang, Y.; Pal, S.; Lin, X.; Bakuru, V. R.; Rambabu, D.; Beljonne, D.; Dincă, M.; Vlad, A. Controlling Charge Transport in 2D Conductive MOFs−The Role of Nitrogen-Rich Ligands and Chemical Functionality. *J. Am. Chem. Soc.* **2023**, *145* (45), 24669−24677.

(17) Jiang, Y.; Oh, I.; Joo, S. H.; Buyukcakir, O.; Chen, X.; Lee, S. H.; Huang, M.; Seong, W. K.; Kwak, S. K.; Yoo, J.-W.; Ruoff, R. S. Partial Oxidation-Induced Electrical Conductivity and Paramagnetism in a Ni(II) Tetraaza[14]Annulene-Linked Metal Organic Framework. *J. Am. Chem. Soc.* **2019**, *141* (42), 16884−16893.

(18) Liu, L.; DeGayner, J. A.; Sun, L.; Zee, D. Z.; Harris, T. D. Reversible Redox Switching of Magnetic Order and Electrical Conductivity in a 2D Manganese Benzoquinoid Framework. *Chem. Sci.* **2019**, *10* (17), 4652−4661.

(19) Darago, L. E.; Aubrey, M. L.; Yu, C. J.; Gonzalez, M. I.; Long, J. R. Electronic Conductivity, Ferrimagnetic Ordering, and Reductive Insertion Mediated by Organic Mixed-Valence in a Ferric Semiquinoid Metal−Organic Framework. *J. Am. Chem. Soc.* **2015**, *137* (50), 15703−15711.

(20) Manini, P.; d'Ischia, M.; Milosa, M.; Prota, G. Acid-Promoted Competing Pathways in the Oxidative Polymerization of 5,6-Dihydroxyindoles and Related Compounds: Straightforward Cyclotrimerization Routes to Diindolocarbazole Derivatives. *J. Org. Chem.* **1998**, *63* (20), 7002−7008.

(21) Connelly, N. G.; Geiger, W. E. Chemical Redox Agents for Organometallic Chemistry. *Chem. Rev.* **1996**, *96* (2), 877−910.

(22) Shannon, R. D. Revised Effective Ionic Radii and Systematic Studies of Interatomic Distances in Halides and Chalcogenides. *Acta Crystallogr., Sect. A* **1976**, *32* (5), 751−767.

(23) Biesinger, M. C.; Lau, L. W. M.; Gerson, A. R.; Smart, R. St. C. Resolving Surface Chemical States in XPS Analysis of First Row Transition Metals, Oxides and Hydroxides: Sc, Ti, V, Cu and Zn. *Appl. Surf. Sci.* **2010**, *257* (3), 887−898.

(24) Dhumal, N. R.; Singh, M. P.; Anderson, J. A.; Kiefer, J.; Kim, H. J. Molecular Interactions of a Cu-Based Metal−Organic Framework with a Confined Imidazolium-Based Ionic Liquid: A Combined Density Functional Theory and Experimental Vibrational Spectroscopy Study. *J. Phys. Chem. C* **2016**, *120* (6), 3295−3304.

(25) Stolz, R. M.; Mahdavi-Shakib, A.; Frederick, B. G.; Mirica, K. A. Host−Guest Interactions and Redox Activity in Layered Conductive Metal−Organic Frameworks. *Chem. Mater.* **2020**, *32* (18), 7639−7652.

(26) Misumi, Y.; Yamaguchi, A.; Zhang, Z.; Matsushita, T.; Wada, N.; Tsuchiizu, M.; Awaga, K. Quantum Spin Liquid State in a Two-Dimensional Semiconductive Metal−Organic Framework. *J. Am. Chem. Soc.* **2020**, *142* (39), 16513−16517.

(27) Felix, C. C.; Sealy, R. C. O-Benzosemiquinone and Its Metal Chelates. Electron Spin Resonance Investigation of Radicals from the Photolysis of Catechol in the Presence of Complexing Metal Ions. *J. Am. Chem. Soc.* **1982**, *104* (6), 1555−1560.

(28) Jiang, Q.; Xiong, P.; Liu, J.; Xie, Z.; Wang, Q.; Yang, X.-Q.; Hu, E.; Cao, Y.; Sun, J.; Xu, Y.; Chen, L. A Redox-Active 2D Metal−Organic Framework for Efficient Lithium Storage with Extraordinary High Capacity. *Angew. Chem., Int. Ed.* **2020**, *59* (13), 5273−5277.

(29) Gu, S.; Wu, S.; Cao, L.; Li, M.; Qin, N.; Zhu, J.; Wang, Z.; Li, Y.; Li, Z.; Chen, J.; Lu, Z. Tunable Redox Chemistry and Stability of Radical Intermediates in 2D Covalent Organic Frameworks for High Performance Sodium Ion Batteries. *J. Am. Chem. Soc.* **2019**, *141* (24), 9623−9628.

(30) Hoshino, N.; Akutagawa, T. A Trinuclear Iron(III) Complex of a Triple Noninnocent Ligand for Spin-Structured Molecular Conductors. *Chem.—Eur. J.* **2018**, *24* (72), 19323−19331.

(31) Torrance, J. B.; Scott, B. A.; Welber, B.; Kaufman, F. B.; Seiden, P. E. Optical Properties of the Radical Cation Tetrathiafulvalenium (TT F +) in Its Mixed-Valence and Monovalence Halide Salts. *Phys. Rev. B* **1979**, *19* (2), 730−741.

(32) Skorupskii, G.; Dincă, M. Electrical Conductivity in a Porous, Cubic Rare-Earth Catecholate. *J. Am. Chem. Soc.* **2020**, *142* (15), 6920−6924.

(33) Skorupskii, G.; Trump, B. A.; Kasel, T. W.; Brown, C. M.; Hendon, C. H.; Dincă, M. Efficient and Tunable One-Dimensional Charge Transport in Layered Lanthanide Metal−Organic Frameworks. *Nat. Chem.* **2020**, *12* (2), 131−136.

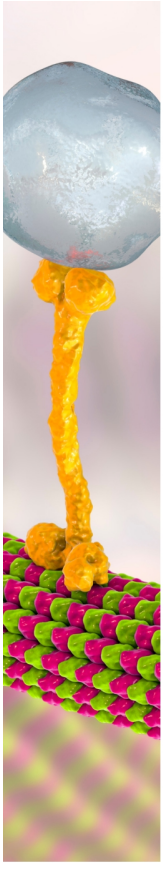
(34) Ohkubo, E.; Suzuki, M.; Aizawa, N.; Ikeda, O.; Kitajima, S.; Koganezawa, T.; Ohta, K.; Oka, K.; Tohnai, N.; Tominaga, K.; Nakayama, K. Highly Porous, Electrically Conductive Two-Dimensional Nickel−Hexaaminodehydrobenzoannulene Frameworks. *J. Am. Chem. Soc.* **2025**, *147*, 31940.

(35) Foster, M. E.; Sohlberg, K.; Allendorf, M. D.; Talin, A. A. Unraveling the Semiconducting/Metallic Discrepancy in Ni3(HITP)-2. *J. Phys. Chem. Lett.* **2018**, *9* (3), 481−486.

(36) Bumberger, A. E.; Nenning, A.; Fleig, J. Transmission Line Revisited − the Impedance of Mixed Ionic and Electronic Conductors. *Phys. Chem. Chem. Phys.* **2024**, *26* (21), 15068−15089.

https://doi.org/10.1021/jacs.5c18105
J. Am. Chem. Soc. 2026, 148, 4339−4348

(37) Hubble, D.; Brown, D. E.; Zhao, Y.; Fang, C.; Lau, J.; McCloskey, B. D.; Liu, G. Liquid Electrolyte Development for Low-Temperature Lithium-Ion Batteries. *Energy Environ. Sci.* **2022**, *15* (2), 550−578.
(38) Wrogemann, J. M.; Lüther, M. J.; Bärmann, P.; Lounasvuori, M.; Javed, A.; Tiemann, M.; Golnak, R.; Xiao, J.; Petit, T.; Placke, T.; Winter, M. Overcoming Diffusion Limitation of Faradaic Processes: Property-Performance Relationships of 2D Conductive Metal-Organic Framework Cu3(HHTP)2 for Reversible Lithium-Ion Storage. *Angew. Chem., Int. Ed.* **2023**, *62* (26), No. e202303111.
(39) Gu, S.; Bai, Z.; Majumder, S.; Huang, B.; Chen, G. Conductive Metal−Organic Framework with Redox Metal Center as Cathode for High Rate Performance Lithium Ion Battery. *J. Power Sources* **2019**, *429*, 22−29.
(40) Zasada, L. B.; Guio, L.; Kamin, A. A.; Dhakal, D.; Monahan, M.; Seidler, G. T.; Luscombe, C. K.; Xiao, D. J. Conjugated Metal−Organic Macrocycles: Synthesis, Characterization, and Electrical Conductivity. *J. Am. Chem. Soc.* **2022**, *144* (10), 4515−4521.
(41) Lin, X.; Apostol, P.; Xu, H.; Bakuru, V. R.; Guo, X.; Chen, Z.; Rambabu, D.; Pal, S.; Tie, D.; Zhang, Y.; Xie, X.; Kim, S.-G.; Li, Y.; Li, Z.; Du, M.; Yan, S.; Zhang, X.; Yuan, R.; Zheng, M.; Gauthy, F.; Finsy, V.; Zou, J.; Gohy, J.-F.; Dong, Q.; Vlad, A. Design Principles of Quinone Redox Systems for Advanced Sulfide Solid-State Organic Lithium Metal Batteries. *Adv. Mater.* **2024**, *36* (32), 2312908.


CAS BIOFINDER DISCOVERY PLATFORM™
BRIDGE BIOLOGY AND CHEMISTRY FOR FASTER ANSWERS
Analyze target relationships, compound effects, and disease pathways
Explore the platform
CAS
A division of the American Chemical Society

https://doi.org/10.1021/jacs.5c18105
J. Am. Chem. Soc. 2026, 148, 4339−4348